Asociación Argentina
de Mecánica Computacional

Mecánica Computacional Vol XXXIV, págs. 75-88 (artículo completo)
Sebastián Giusti, Martín Pucheta y Mario Storti (Eds.)
Córdoba, 8-11 Noviembre 2016

MATERIAL POINT METHOD (MPM) ANALYSIS OF HYDRODYNAMIC IMPACT PROBLEMS INVOLVING EMBEDDED SOLIDS

Krishnendu Shekhar[a], Wen-Chia Yang[a], Pedro Arduino[b], Peter Mackenzie-Helnwein[b] and Greg Miller[b]

[a]*Graduate Student, Department of Civil and Environmental Engineering, University of Washington, Seattle, WA 98195-2700, United States*

[b]*Faculty, Department of Civil and Environmental Engineering, University of Washington, Seattle, WA 98195-2700, United States*

Keywords: Material Point Method; Debris; Fluid; Impact; Tsunami; Bridge; Fluid-solid interaction

Abstract. Impact of debris carried by floods or tsunamis can cause severe damage to bridges, though they are not well studied in the literature. The Material Point Method (MPM) provides a framework for modeling such systems involving combined fluid/solid behavior with complex interactions. Conventional MPM uses regular grids with tri-linear interpolation. However, linear functions introduce volumetric locking for (nearly) incompressible materials, posing problems when modeling fluids. To eliminate locking, nodebased, cellbased and hybrid formulations were adapted by Mast et al., *J. Comp. Phys., Vol. 231, pp 5351–5373, (2012)*. In this paper we propose a new numerical flux smoothing algorithm to produce smooth stress fields in complex hydrodynamic problems while ensuring numerical stability. The goal is not only to produce strain and stress fields free of locking, but also to stabilize high frequency numeric oscillation. The improved algorithms are applied to fluid driven debris impact problems, and validated against experimental results. Emphasis is in given to evaluating demands on bridge superstructures by tsunami driven debris.

Copyright © 2016 Asociación Argentina de Mecánica Computacional http://www.amcaonline.org.ar

1 INTRODUCTION

Throughout history, strong earthquakes have struck countries all over the world and caused major damage. Most of this damage has been due to ground shaking, but in coastal areas tsunamis induced by earthquakes have resulted in greater loss of lives and infrastructure. As coastal populations continue to increase around the world, understanding and managing tsunami effects on infrastructure becomes increasingly important.

The objective of this study is to give preliminary results for researchers and engineers trying to understand the demands on bridge superstructures by tsunami-driven debris. In this research the material point method (MPM) is used to model these complex fluid/solid (moving and stationary) interactions.

The standard MPM implementation uses a regular orthogonal grid with tri-linear shape functions. While this is not the only variant in use (see, e.g., Lim et al. (2013)), it remains popular for its simplicity. However, the linear shape functions also introduce not only volumetric locking for (nearly) incompressible materials (hence causing problems when modeling liquids), but also integration errors, which arise from the MPM particle discretization. Each of these issues is problematic, and must be addressed to generate useful solutions.

The ultimate goal of the work is to model tsunami induced debris impacts in three dimensions like shown in Figure 1 and to understand damming and more complex flows around the superstructure during a tsunami. The results presented in this study are obtained using a single-threaded MPM code. This limits the mesh and particle refinements used in the validation examples and the debris-induced load study is relatively coarse compared to general applications found in the literature.

2 ANTI-LOCKING STRATEGY

The anti-locking strategy employed is based on the Hu-Washizu principleHu (1954); Washizu (1982). It is expressed as a set of weak form equations:

$$\int_\Omega \rho\delta\tilde{\bar{\boldsymbol{\sigma}}} : \left(\boldsymbol{d} - \tilde{\boldsymbol{d}}\right)\, dV = 0 \quad , \qquad \int_\Omega \delta\tilde{\boldsymbol{d}} : \rho\left(\bar{\boldsymbol{\sigma}} - \tilde{\bar{\boldsymbol{\sigma}}}\right)\, dV = 0 \tag{1}$$

and

$$\int_\Omega \delta\boldsymbol{v} \cdot \rho\boldsymbol{a}\, dV = -\int_\Omega \operatorname{grad}\delta\boldsymbol{v} : \rho\tilde{\bar{\boldsymbol{\sigma}}}\, dV + \int_\Omega \delta\boldsymbol{v} \cdot \rho\bar{\boldsymbol{b}}\, dV + \int_{\partial\Omega^\tau} \boldsymbol{\tau}^* \cdot \delta\boldsymbol{v}\, dS \tag{2}$$

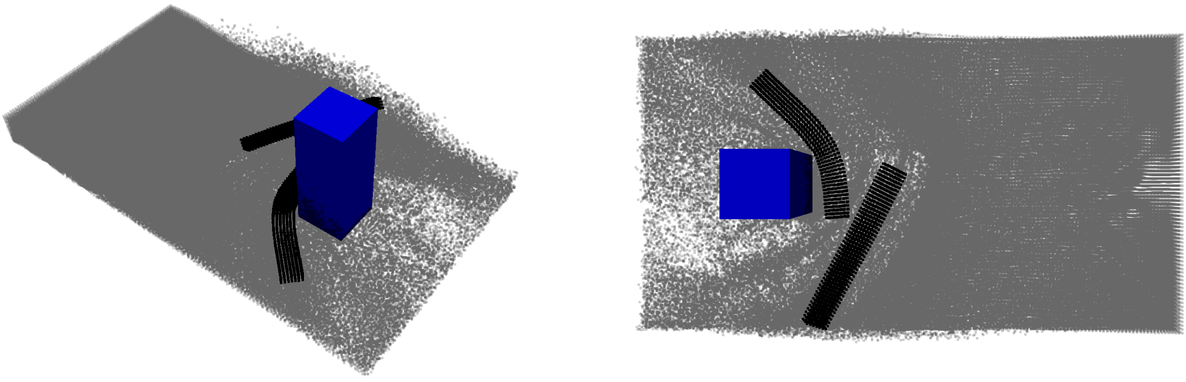

(a) (b)

Figure 1: 3-D simulation of two pieces to debris impacting a column causing partial damming

Copyright © 2016 Asociación Argentina de Mecánica Computacional http://www.amcaonline.org.ar

where ρ is mass density, $\boldsymbol{v}$ is the velocity field, $\boldsymbol{a}$ is the acceleration field, $\boldsymbol{\tau}^*$ a prescribed surface traction, $\boldsymbol{d} = \frac{1}{2}(\operatorname{grad}\boldsymbol{v} + \operatorname{grad}^T\boldsymbol{v})$ is the rate of deformation tensor, $\bar{\boldsymbol{\sigma}} = \boldsymbol{\sigma}/\rho$ is the mass-specific stress, all defined in the physical space, and $\delta\boldsymbol{v}$, $\delta\tilde{\boldsymbol{d}}$, $\delta\tilde{\bar{\boldsymbol{\sigma}}}$ are weight functions defined on the background grid. The improved rate of deformation, $\tilde{\boldsymbol{d}}$, and the improved specific stress, $\tilde{\bar{\boldsymbol{\sigma}}}$, are defined as piece-wise constant functions in this study and represent the locking-free solution (one-point quadrature elements). The algorithm is implemented in an updated Lagrangian framework and is very similar to the $[\mathbb{P}_1]^3/\mathbb{P}_0$ interpolation discussed in Süli (2013) and thus shares concerns regarding spurious modes (checker-boarding) due to a violation of the LBB-condition Süli (2013); Bathe (2001). We address the issue by introducing numeric dissipation through smoothing.

Following the framework of the cell-based antilocking algorithm proposed by Mast et al. (2012), at any n-th time step Equation (2) yields modified nodal internal forces $\boldsymbol{f}_i^{int(n)}$:

$$\boldsymbol{f}_i^{int(n)} = -\sum_p m_p \tilde{\bar{\boldsymbol{\sigma}}}_p^{(n)} \cdot \operatorname{grad} N_i(\boldsymbol{x}_p^{(n)}) \tag{3}$$

in which i is the node index, p is the particle index, m_p is the particle mass, $\boldsymbol{x}_p$ are the particle coordinates, and N_i represents the shape functions. Particles in any cell c are then updated with the improved fields $\tilde{\boldsymbol{d}}_c$ and $\tilde{\bar{\boldsymbol{\sigma}}}_c$ at the end of the n-th time step using Equation (1):

$$\tilde{\boldsymbol{d}}_c^{(n+1)} = \frac{1}{m_c}\sum_{p\in\Omega_c} m_p \boldsymbol{d}_p^{(n+1)} \quad , \qquad \tilde{\bar{\boldsymbol{\sigma}}}_c^{(n+1)} = \frac{1}{m_c}\sum_{p\in\Omega_c} m_p \bar{\boldsymbol{\sigma}}_p^{(n+1)} \tag{4}$$

in which Ω_c represents the domain of cell c and $m_c = \sum_{p\in\Omega_c} m_p$ the mass contained in that domain. The reader is referred to Mast et al. (2012) and Yang (2016) for a full discussion of these expressions.

3 LIMITED CONSTANT FLUX SMOOTHING ALGORITHM

MPM uses material points directly as integration points, which like any discretization introduce integration errors. Because the location of these integration points follow the material motions, they are not optimized for integration accuracy. The associated integration errors can result in nonphysical unbalanced nodal loads when the stress fields are discontinuous across cell boundaries. These spurious forces cause high frequency stress field checkerboarding and system destabilization, which is difficult to control with most existing stabilization strategies for one-point quadrature elements. In this work, following the previous work in Mast et al. (2012), we propose an improved smoothing approach based on a limited constant flux smoothing algorithm, separately applied on each state variable at each time step before particle updating. This reduces the effects of the integration errors by means of a diffusive mechanism. Due to space constraints, only the essential idea is presented here. A complete derivation and discussion can be found in Yang[7].

4 VALIDATION EXAMPLE

A rectangular tank half filled with fluid at rest in stable equilibrium (i.e., the initial conditions should match the solution at any time, t) is used to study the performance of the new proposed smoothing algorithm. The simulation is simplified as a plane strain problem, in which the fluid has a bulk modulus $K = 2.2\,\mathrm{GPa}$, mass density $\rho = 1000\,\mathrm{kg/m^3}$ and viscosity $\mu = 0.001\,\mathrm{Pa\cdot s}$. Acceleration due to gravity is $g = 10\,\mathrm{m/s^2}$. The tank has a width of 3.2 m and a height of 6.4 m.

Copyright © 2016 Asociación Argentina de Mecánica Computacional http://www.amcaonline.org.ar

For all plane-strain models considered in this validation, the boundary condition for the tank's inner surfaces is

$$\boldsymbol{v}_i^{(n+1)} \cdot \boldsymbol{n}_i = 0, \text{ if } \boldsymbol{v}_i^{(n+1)} \cdot \boldsymbol{n}_i < 0 \tag{5}$$

and unconstrained otherwise. $\boldsymbol{v}$ is the velocity, $\boldsymbol{n}$ is the unit normal to the inner surface of the tank; a superscript $(n+1)$ indicates time t_{n+1}; and a subscript i represents node i on the grid. The rotation angle θ_g of the computational grid is selected as 0 ° (which is aligned with the rectangular tank) and 45 ° relative to the tank floor. θ_g = 45 ° is used to intentionally introduce integration errors into the simulation so that capabilities of the smoothing algorithms in handling destabilizing sources derived from integration errors can be tested. To do so, an enhanced boundary treatment developed by Yang (2016) is used to decouple the grid geometry from the boundary geometry. The numbers of particles per cell (ppc) and cells per length (cpl) are used to quantify any level of refinement. Equivalent ppc and cpl values obtained for models with θ = 0 ° are used to indicate refinement levels for models with θ_g = 45 °, in which grid lines are not parallel to the edges of the square water block and hence cells do not necessarily have the same number of particles. Simulation duration is taken as 3 seconds (simulated physical time), which allows the fluid block to have visible motion, if any, regardless of the cause of this non-physical behavior.

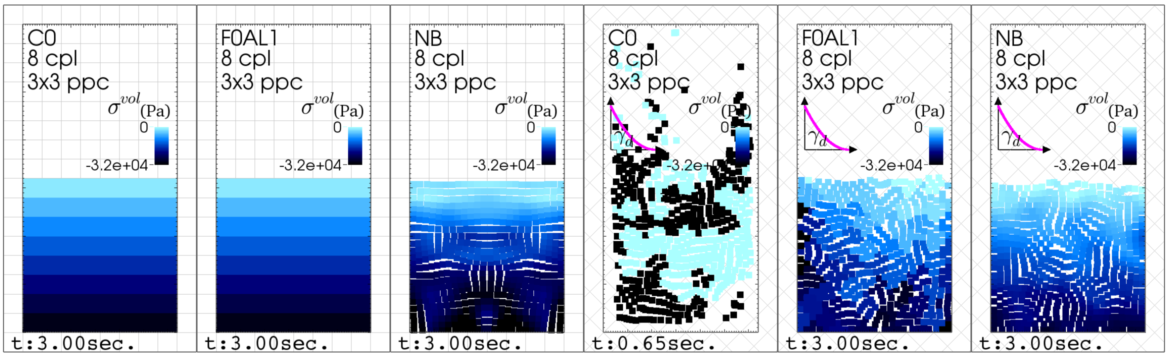

(a) (b) (c) (d) (e) (f)

Figure 2: Comparison of simulation snapshots between C0, F0AL1 and NB algorithms with grid orientation θ_g = (a) 0 ° and (b) 45 °

The first test is designed to show a strong dissipative characteristic of the node-based algorithm (NB)Mast et al. (2012). Grid orientation is selected as θ_g = 0 ° to fit the geometry of the water tank, and 8 cells per length (of the square fluid block) and 3×3 particles per cell are used. Figure 2(a) compares the simulation results using the cell-based approach (C0), the limited constant flux algorithm (F0AL1), and the node-based approach (NB) at $t = 3\,\mathrm{s}$. It shows both C0 and F0AL1 can keep the same stress field till the end of the simulations at 3 seconds. In contrast, NB over-smooths the stress field and changes the equilibrium status even though it generates the desired continuous stress field. This artificial change of the stress field causes global unbalanced downward forces and hence introduces a non-physical reduction of volume (height).

Next, the same setup as the first test is used except the grid is rotated by 45 ° counterclockwise around the left bottom corner of the fluid tank. Figure 2(b) shows the cell-based algorithm (C0) is not able to sufficiently control the destabilization caused by integration errors due to unfavorable placement of the particles for integration purposes, and hence the simulation fails,

Copyright © 2016 Asociación Argentina de Mecánica Computacional http://www.amcaonline.org.ar

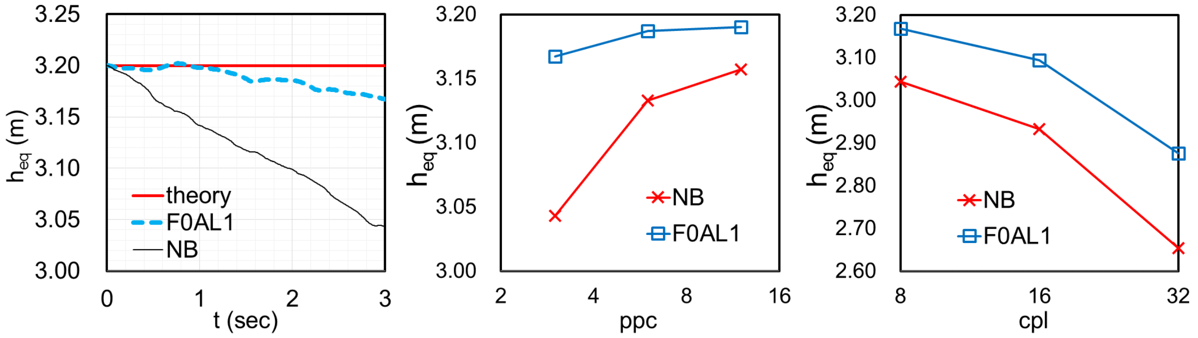

(a) (b) (c)

Figure 3: Equivalent height h_{eq}: (a) time history (8 cpl, 3^2 ppc), (b) influence of ppc refinement (8 cpl); and (c) influence of cpl refinement (3 ppc).

showing dramatic numeric instabilities. Consistent with its design, the limited constant flux algorithm (F0AL1) stabilizes the simulation through artificial diffusion and dissipation of energy, very similar to the node-based algorithm (NB). Both F0AL1 and NB algorithms suffer from non-physical loss of volume. However, with the flux limiter, F0AL1 significantly reduces the non-physical volume (height) changes as presented in the time history graphs of the equivalent height, h_{eq}, in Figure 3a. Figure 3b shows that this non-physical behavior can be controlled by increasing the number of particle per cell (ppc), (i.e., by reducing the integration error). However, Figure 3c demonstrates for this test problem that refining the grid at constant ppc increases the sources of destabilization, which triggers more energy dissipation for stabilization, and, consequently, exacerbates the non-physical behavior.

In summary, the MPM enhanced by the proposed smoothing (stabilizing) algorithm has been tested with a hydrostatic problem, water in a rectangular tank. The results show that (1) unlike C0 and F0AL1, NB includes a spurious mode and cannot sustain a static equilibrium state for water even if there is no integration error in the calculation; (2) the integration error induced by the MPM particle forms is a source of destabilization, which caused the C0 simulations to become unstable; (3) both F0AL1 and NB can handle the destabilization caused by the integration error through introducing algorithmic diffusion and thus dissipation; (4) F0AL1 offers a control mechanism for the algorithmic diffusion that NB does not possess; (5) increasing the number of particles per cell controls the integration error (i.e., the destabilizing source); and (6) grid refinement can also introduce destabilization due to motion of particles and cell crossing, and thus will not necessarily increase the accuracy of a simulation.

5 APPLICATION TO DYNAMIC FLUID-SOLID INTERACTION

A complex fluid-solid-interaction simulation is used to demonstrate the capability of the limited constant flux smoothing algorithm (F0AL1) to handle integration-error-induced destabilization. The problem consists of a floating square block, free to move in a tank as shown in Figure 4a. The tank will be filled with fluid, forcing interaction with the tank's walls, as well as fluid-solid interaction with the block.

Fluid is injected from the left at a constant height of 1.0 m at an initial velocity of $v_0 = 1.0\,\mathrm{m/s}$. The inflow of water continues for a duration of $6.0\,\mathrm{s}$, after which the inflow ceases completely. The mass density of the fluid matches that of water: $\rho_w = 1000\,\mathrm{kg/m^3}$, while that of the solid is $\rho_s = 300\,\mathrm{kg/m^3}$. To decrease computational time by controlling the speed

Copyright © 2016 Asociación Argentina de Mecánica Computacional http://www.amcaonline.org.ar

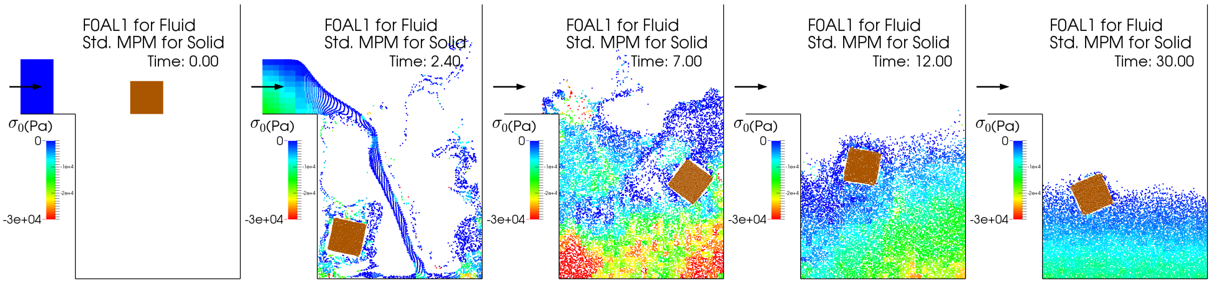

(a) (b) (c) (d) (e)

Figure 4: Simulated means stress (negative pressure) distribution in the fluid using the limited constant numerical flux smoothing (F0AL1). (a) Initial conditions, (b)–(e) after 2.4 s, 7.0 s, 12.0 s, and 30.0 s, respectively.

of sound in the fluid, a bulk modulus smaller than that of water is used, $K = 20\,\mathrm{MPa}$, and the viscosity is $\mu = 0.001\,\mathrm{Pa{\cdot}s}$. The solid block measures $0.4\,\mathrm{m} \times 0.4\,\mathrm{m}$ with elastic modulus $E_s = 1\,\mathrm{MPa}$ and Poisson's ratio $\nu_s = 0.25$. The tank has a width of $3\,\mathrm{m}$ and a height of $3\,\mathrm{m}$ on the left side, while offering infinite height on the right. The regular computational grid is made of square cells of $0.1\,\mathrm{m} \times 0.1\,\mathrm{m}$.

The solid block is released at $t = 0$ s and falls under gravity, then is dragged to the left and lifted up from the bottom by the injected water as shown in Figure 4b. The injection causes turbulence dragging the block left and right under water (Figure 4c) until the block floats up to the surface (Figure 4d) and stays afloat to the end of the simulation (Figure 4e).

Figure 4 also shows the computed mean stress (negative of pressure) for the same states. Throughout the simulation, free surface conditions ($p = 0$ MPa) are satisfied. The pressure field in the fluid is reasonably smooth, showing only minor artifacts from the underlying grid. Peak pressure corresponds close to the hydrostatic pressure of $30\,\mathrm{kPa}$ at $t = 7.0$ s, $20{-}25\,\mathrm{kPa}$ at $t = 12$ s, and $15\,\mathrm{kPa}$ at $t = 30$ s.

Figure 4e also illustrates the remaining issue of smoothing algorithms: the cell-based, node-based, and the limited constant flux algorithms all artificially dissipate strain energy over time when integration errors exist, and this results in compaction of the particles. The amount of fluid in the analysis should fill the tank to 2/3 of its height. This is approximately the case at $t = 12$ s, but is noticeable violated by $t = 30$ s. This side-effect is also visible for quasi static states after a large number of time steps (3×10^7 steps at $t = 30$ s). However, the task of eliminating this error remains open for future improvements.

Overall, these results demonstrate that the limited constant flux algorithm is able to stabilize a complex hydrodynamic analysis involving splashing fluid and complex fluid-solid interaction, and hence is capable of handling tsunami-debris-structure interactions, albeit with some non-physical loss of fluid volume.

6 TSUNAMI FLUME EXPERIMENTS

In an effort to show the applicability of the method to capture the response of fluids and the effect of tsunami induced forces, MPM simulation results were compared with experimental results.

Experiments were conducted at the Charles W. Harris Hydraulics Laboratory of the University of Washington to study the impact of a bore of water on a stationary column. The wave tank was 16.62 m long, 0.61 m wide and 0.45 m deep.

Copyright © 2016 Asociación Argentina de Mecánica Computacional http://www.amcaonline.org.ar

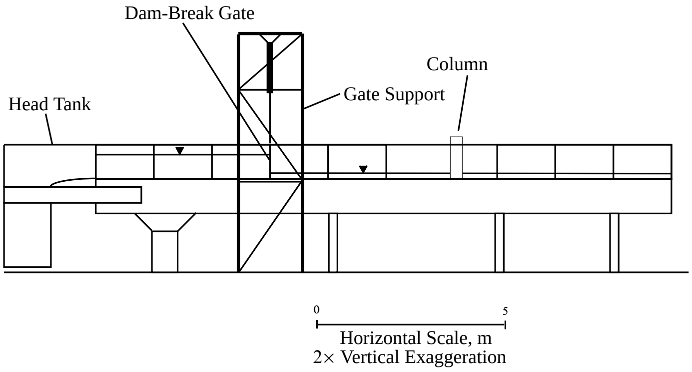

Figure 5: Schematic of the experimental setup

ÃĄrnason (2005)

The wave is generated by lifting the dam-break-gate and allowing the water in the head tank to flow into the channel. The properties of the wave thus generated can be controlled by the height of the water in the head tank and the height of water in the channel. ÃĄrnason (2005)

The parameters used to validate our simulation done using MPM are the velocity of the water, the height of the water and the force on the column. The velocity is noted at a point in the upstream face of the column, however in the absence of the column. This is done on the assumption that the size of the column is small enough compared to the width of the channel to not affect the flow of the water in any significant manner. The height is measured at a point equidistant from the outer edge of the column and the inner surface of the channel.

7 SIMULATION SETUP

In order to minimize the processing time while retaining the ability to produce reasonably accurate results, only a small part of the entire channel around the column is simulated as shown in Figure 6a.

To the left of the simulation domain as shown in Figure 6a the Reimann solution for the dam break problem problem as an input by generating a stream of particles and pushing them into the domain at a pre-calculated velocity.

The particles which have already passed the column are destroyed to the right of the simulation domain. This helps us to make the simulation computationally less intensive.

8 EFFECT OF CELL SIZE

It is clearly visible from Figure 6b that the refinement of the computational grid has a very significant effect on the accuracy of the simulations. As can be seen, the forces from the simulations match pretty decently with the experimental results at a cell size of $0.015m$. Refinement of the grid has a dramatic effect on the noise generated in the simulation results. Also, we can conclude that the accuracy of the results also improve significantly if the mesh is refined.

9 TESTING OF THE ARBITRARY BOUNDARY

In order to convince ourselves that our methodology is objective, we conducted simulations for a column rotated by $45°$ for which experimental results were also available. Since the boundaries that define the column are no longer defined along the mesh lines, the column has to be modeled using arbitrary boundaries. This transformation is shown in Figure 7 and comparison of simulated and recorded forces on the column are shown in Figure 8.

Copyright © 2016 Asociación Argentina de Mecánica Computacional http://www.amcaonline.org.ar

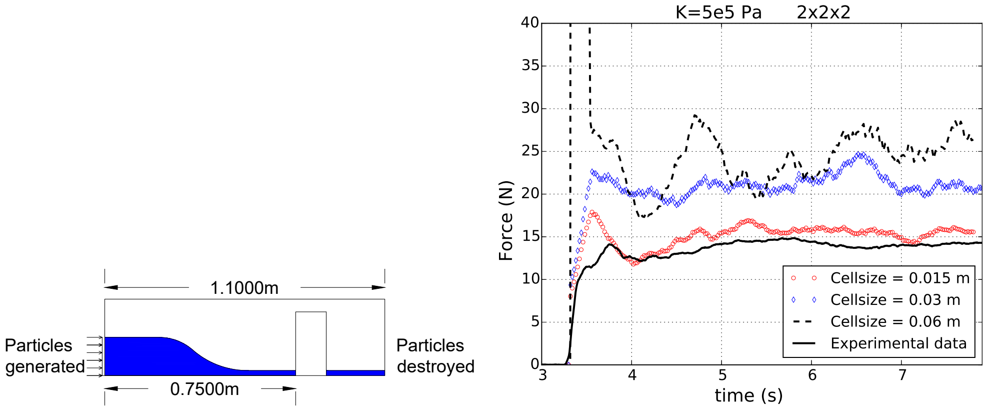

(a) (b)

Figure 6: (a) Simulation domain and (b) results for K = $5e^5$ Pa

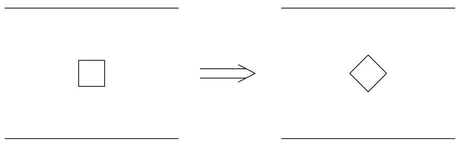

Figure 7: Transformation

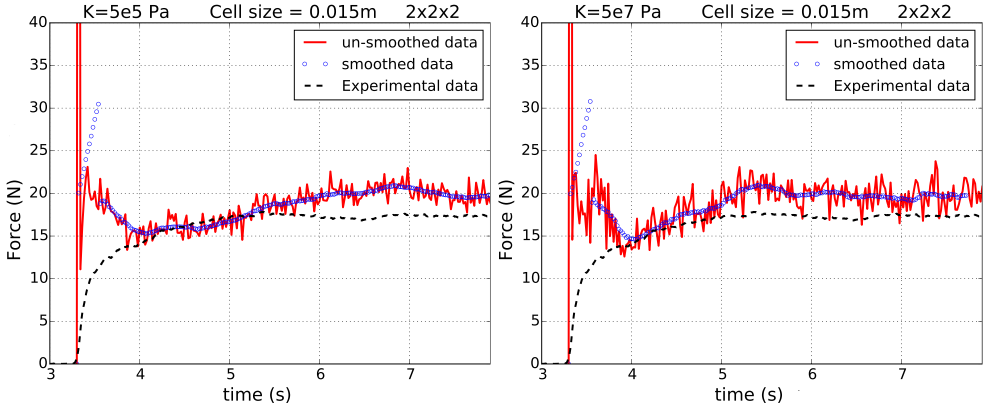

(a) (b)

Figure 8: Forces for different fluid bulk modulus(K) (a)K = $5e^5$ Pa (b)K = $5e^7$ Pa

Copyright © 2016 Asociación Argentina de Mecánica Computacional http://www.amcaonline.org.ar

10 EVALUATION OF DEBRIS IMPACT FORCES

10.1 Debris loads

Debris carried by flowing water can induce loads higher than hydrostatic and kinematic forces induced by flowing water alone. Keeping this perspective in mind, ASCE-7-16 attempts to predict debris induced forces. In this research we compare the equations provided by ASCE with MPM simulation results. We conduct a set of simulations of in-air cases(only debris, in the absence of a carrying fluid) and then we conduct a set of simulations in-water case(debris being carried by fluid).

The equations provided in the ASCE-7-16 draft proposal are provided in Equations 6 and 7. Equation 6 can be considered as the analytical solution to an impact problem resulting in complete loss of momentum for a moving object. Equation 6 gives a relationship where modifiers I_{tsu} and C_o are used to provide practical results.

$$F_{ni} = u_{max}\sqrt{km_d} \tag{6}$$

$$F_i = I_{tsu}C_oF_{ni} \tag{7}$$

where:
C_o is the orientation coefficient equal to 0.65 for logs and poles,
u_{max} is the maximum flow velocity at the site occurring at depths sufficient to float the debris,
I_{tsu} is the tsunami Importance factor as provided in table 1
m_d is the mass W_d/g of the debris
k is the effective stiffness of the impacting debris or the lateral stiffness of the impacted structural element(s) deformed by the impact, whichever is less

Tsunami Risk Category	I_{tsu}
II	1.0
III	1.25
IV	1.25
Vertical Evacuation Refuges	1.25
Category III Critical Facilities	1.25

Table 1: Tsunami Importance Factors for Hydrodynamic and Impact Loads

The effective stiffness k is calculated by considering the projected area of the debris on the column

$$k = \frac{EA}{L} \tag{8}$$

Impulse duration for an elastic impact has been calculated as:

$$t_d = \frac{2m_du_{max}}{F_{ni}} \tag{9}$$

ASCE-7 prescribes that for an equivalent elastic static analysis, the impact force shall be multiplied by the dynamic response factor R_{max}. The relationship between R_{max} and t_d is provided in the table below.

Copyright © 2016 Asociación Argentina de Mecánica Computacional http://www.amcaonline.org.ar

Table 2: Dynamic Response Ratio for Impulsive Loads

t_d/t_n	R_{max}
0.0	0
0.1	0.4
0.2	0.8
$\geq$ 1.4	1.5

where t_n is the natural time period of the structure
Note: The table has been truncated. For the full table please refer ASCE-7 table 6.11-1.

10.2 Caveats

- A minimum debris weight of 454 kg has been prescribed
- A minimum log stiffness of 6.1×10^7 Pa has been prescribed
- In our simulations the column is modeled as boundaries. Therefore, $t_n \rightarrow 0$. So $t_d/\omega_n \geq 1.4$

11 DEBRIS IMPACT WITHOUT FLOWING WATER

As shown in Figure 9, the debris is oriented with its longer dimension in the direction of motion. The dimension and material properties of the debris are described in table 3. A is the area of impact between the debris and the column. L is the dimension in the direction of velocity of the debris. The debris is released at a certain velocity and the impact force is recorded on the column. The force recorded on the column with the corresponding impact velocity is shown in Figure 10a and Figure 11a. As is evident from Figure 10b and Figure 11b, the simulation forces compare well with the predicted forces from ASCE-7-16 draft.

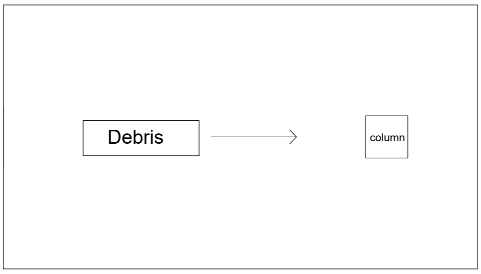

Figure 9: Longitudinally oriented debris

Table 3: Debris Parameters

A	E	L	k	I_{tsu}	C_0
$0.01m^2$	346153.85 Pa	0.33 m	10489.51 Pa.m	1.0	0.65

Copyright © 2016 Asociación Argentina de Mecánica Computacional http://www.amcaonline.org.ar

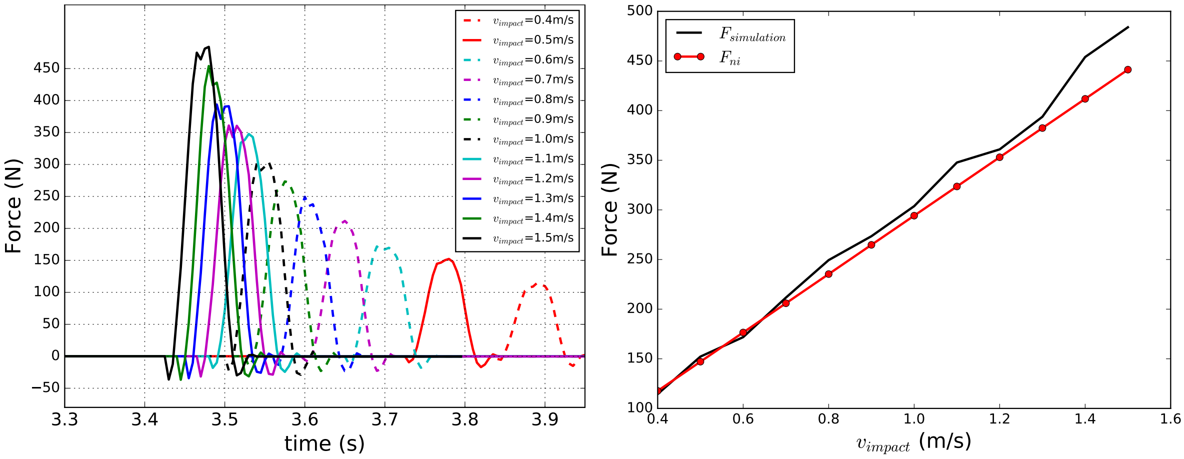

(a) (b)

Figure 10: (a) Relationship between debris impact velocity and force for $\rho = 2500 kg/m^3$ and debris impacting longitudinally and (b) comparision with ASCE-7

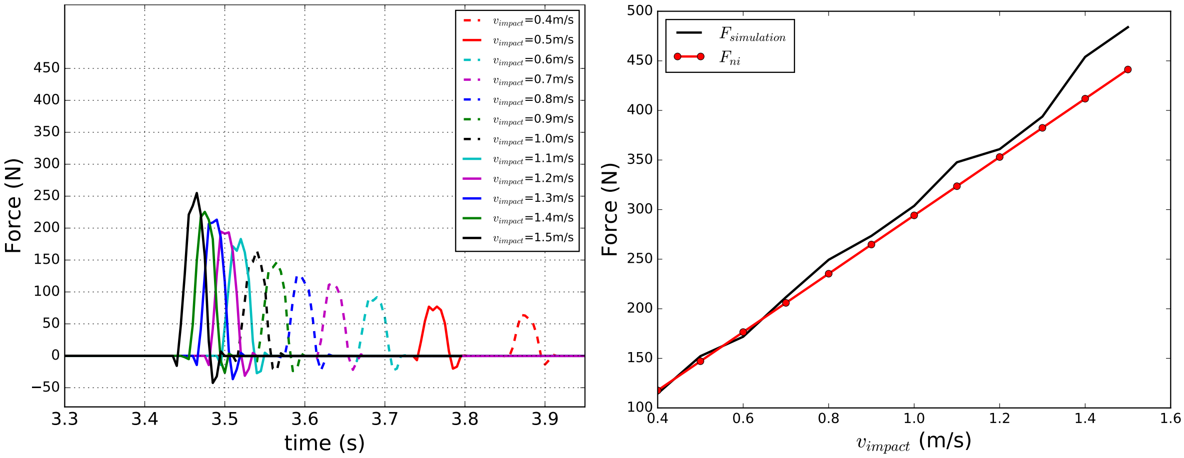

(a) (b)

Figure 11: (a) Relationship between debris impact velocity and force for $\rho = 2500 kg/m^3$ and debris impacting longitudinally and (b) comparision with ASCE-7

Copyright © 2016 Asociación Argentina de Mecánica Computacional http://www.amcaonline.org.ar

12 DEBRIS IN FLOWING WATER

Having conducted simulations for only the tsunami bore and only the debris(in-air case) we need to look into how the simulation forces are influenced when we evaluate the impact forces from debris carried by a tsunami bore(in-water case). For this purpose, we use the same orientation of debris and same fluid and solid parameters.

We find that there is some disagreement between the forces from simulation results shown in Figure 12a and Figure 14a and the analytical force,F_{ni}. Applying the modifiers I_{tsu} and C_o does help to close the gap between the predicted force F_i and the forces recorded from the simulations. Another crucial observation that can be made from the plots in Figure 12b and Figure 14b is that the denser debris loses its velocity at a lower rate compared to the less dense debris. As a result, the discrepancy between the simulated and predicted force is less in case of a denser debris and more in case of a less dense debris as can be seen in Figure 13 and Figure 15.

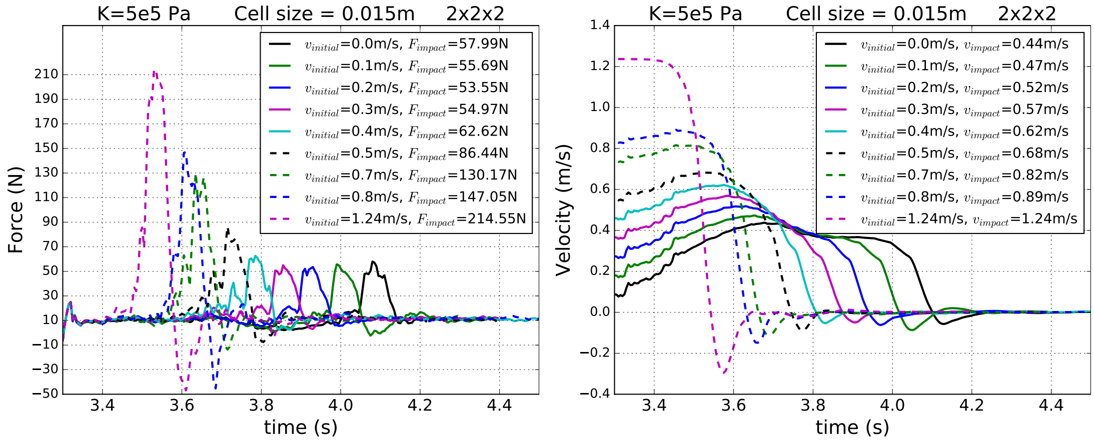

(a) (b)

Figure 12: (a) Forces and (b) velocities for different impact velocities for a debris with $\rho = 2500kg/m^3$

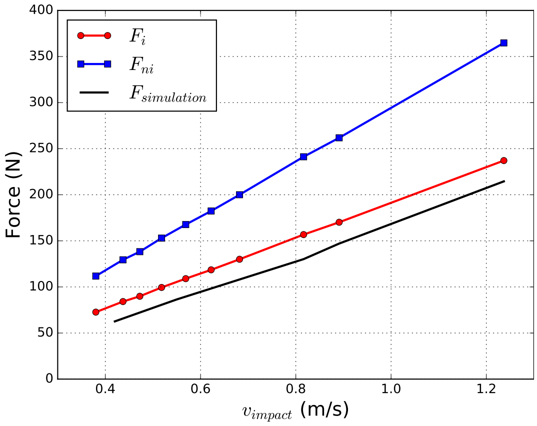

Figure 13: Simulation forces for different impact velocities for a debris with $\rho = 2500kg/m^3$

Copyright © 2016 Asociación Argentina de Mecánica Computacional http://www.amcaonline.org.ar

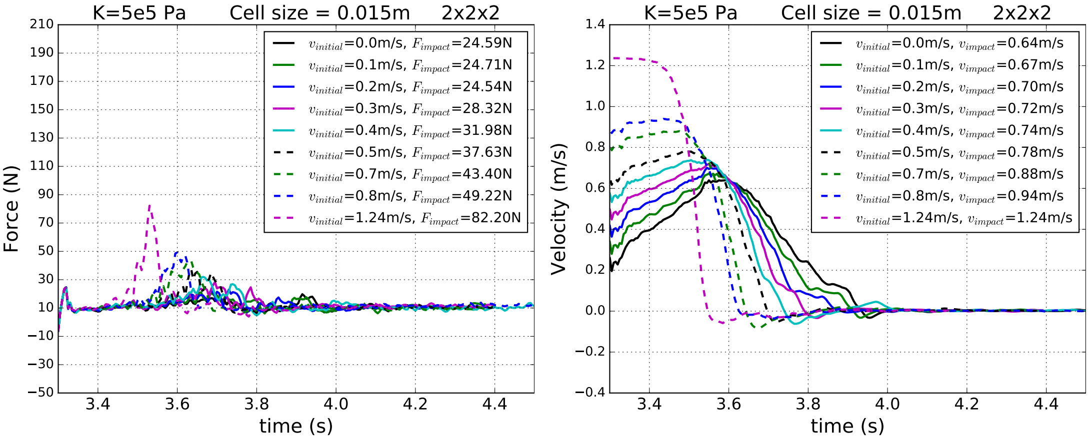

(a) (b)

Figure 14: (a) Forces and (b) velocities for different impact velocities for a debris with $\rho = 750kg/m^3$

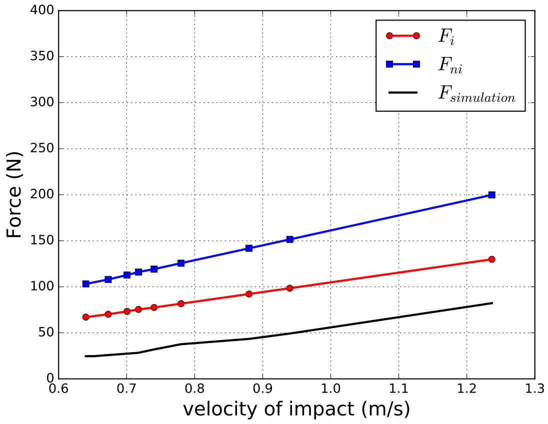

Figure 15: Simulation forces for different impact velocities for a debris with $\rho = 750kg/m^3$

Copyright © 2016 Asociación Argentina de Mecánica Computacional http://www.amcaonline.org.ar

13 SUMMARY AND CONCLUSIONS

In this study, we have discussed the issues with modeling fluids in MPM and some solutions were proposed.

To convince ourselves about the applicability of this technique to model fluids, several validation tests were done by comparing simulation results with flume experiments. We found that using a sensibly fine mesh, we can reasonably predict the force from a tsunami bore impact on a column. Using this result as a base, we introduced debris(solids) to the simulation where we found that results from simulation of in-air cases match analytical equations and ASCE-7-16 recommendations fairy well. However, when the results from simulations where the debris is carried by a tsunami bore are compared with ASCE-7-16 draft provisions, the results differ by some margin. This may be attributed to the fact that complex fluid flow around a structure has a noticeable influence on the impact of the debris with the column. The effect of this flow around the column is relatively less pronounced in case of a denser debris and more pronounced in case of a heavier debris. Further tests are required to accurately judge the motion and the force induced by a debris carried by a tsunami.

REFERENCES

Bathe K.J. The inf – sup condition and its evaluation for mixed finite element methods. *Computer and Structures*, 79(2):243–252, 2001. ISSN 0045-7949. doi:10.1016/S0045-7949(00)00123-1.

Hu H.C. On some variational principles in the theory of elasticity and the theory of plasticity. *Acta Physica Sinica*, 10(3):259–290, 1954.

Lim L., Andreykiv A., and Brinkgreve R. Pile penetration simulation with material point method. In M. Hicks, J. Dijkstra, M. Lloret-Cabot, and M. Karstunen, editors, *Installation Effects in Geotechnical Engineering*, pages 24–30. CRC Press, 2013. doi:10.1201/b13890-5.

Mast C.M., Mackenzie-Helnwein P., Arduino P., Miller G.R., and Shin W. Mitigating kinematic locking in the material point method. *Journal of Computational Physics*, 231(16):5351–5373, 2012. ISSN 0021-9991. doi:10.1016/j.jcp.2012.04.032.

ÃĄrnason H. *Interactions between an Incident Bore and a Free-Standing Coastal Structure*. Ph.D. thesis, University of Washington, 2005.

Süli E. A brief excursion into the mathematical theory of mixed finite element methods. *Lecture Notes, University of Oxford*, pages 24–29, 2013.

Washizu K. *Variational methods in elasticity and plasticity*. Pergamon Press, Oxford, 3 edition, 1982. ISBN 0080267238 9780080267234.

Yang W.C. *Study of Tsunami-Induced Fluid and Debris Load on Bridges using the Material Point Method*. Ph.D. thesis, University of Washington, 2016.

Copyright © 2016 Asociación Argentina de Mecánica Computacional http://www.amcaonline.org.ar